AIAA JOURNAL
Vol. 37, No. 12, December 1999

Three-Dimensional Turbulent Interactions Caused by Asymmetric Crossing-Shock Configurations

D. V. Gaitonde* and J. S. Shang†
U.S. Air Force Research Laboratory, Wright–Patterson Air Force Base, Ohio 45433-7521
T. J. Garrison‡
Louisiana State University, Baton Rouge, Louisiana 70803-6413
and
A. A. Zheltovodov§ and A. I. Maksimov¶
Institute of Theoretical and Applied Mechanics, 630090 Novosibirsk, Russia

A further understanding is developed of the physics of three-dimensional shock-wave/turbulent boundary-layer interactions produced by asymmetric double-fin geometries. A numerical method is employed to reproduce the mean flow of an experimental test matrix of six configurations composed of all combinations of 7-, 11-, and 15-deg fins, yielding interactions of various degrees of asymmetry and strength. The nature of asymmetric interactions is discussed with particular emphasis on the case where the two sharp fins have angles of 7 and 15 deg, respectively. The flowfield can be described in terms of a vortical structure impinging on a side wall and becoming aligned in a direction parallel to it. Details of the shock pattern and vorticity field are correlated with the streamline structure and assimilated within the framework developed in previous work for symmetric interactions. The changes occurring with increasing interaction strength in the total pressure map and vorticity field are elucidated.

Introduction

THE importance of accounting for shock-wave/turbulent boundary-layer interaction (STBLI) phenomena in the design and performance of aircraft components has been recognized in the literature.[1,2] Understanding of the fundamental fluid dynamic mechanisms is greatly facilitated through the use of simple configurations, which may be viewed as building blocks of more complicated practical geometries. Among these canonical shapes is the focus of the present work, the double-fin geometry composed of two fins mounted on a flat plate, as shown in Fig. 1. The configuration is representative of elements of proposed nonaxisymmetric scramjet designs. The flow parameters of interest include the Mach and Reynolds numbers, the features of the incoming boundary layer, the fin angles, the distance between the fins, and the wall thermal conditions. The resultant flowfield has received substantial attention in the last decade, both for symmetric and asymmetric situations at a range of pertinent parameters: a compilation of some numerical efforts may be found in Ref. 3, which is also a rich source of literature on experimental efforts.

The motivation for the present effort stems from Ref. 4, which described the fully separated flowfield produced by a 15×15 deg geometry at Mach 4. Figure 2a shows the principal elements in terms of four regimes: a separated boundary layer, vortex interaction, centerline vortices, and entrainment. The distinct footprint of each regime is shown in Fig. 2b. The several lines of coalescence and divergence observed in Fig. 2b have direct counterparts in experimental observation, as documented previously.[5]

The objective of the present effort is to further extend the understanding of the mean flow with particular emphasis on the nature of shock-induced three-dimensional separation and the resulting establishment of the vorticity field. Toward this end, 1) the structure of highly asymmetric interactions is investigated and assimilated within the framework of Ref. 4, which focused exclusively on symmetric flows, and 2) computations are employed to characterize the effect of interaction strength, adjusted by varying fin angles, on the evolution of the flowfield structure.

Because numerical simulations are a major component of the present study, it is important to evaluate their fidelity to the physics. The literature indicates that, for double-fin interactions, various aspects of the mean flow are reproduced fairly accurately by several popular turbulence models. These aspects include 1) surface pressure,[3] 2) flowfield surveys of pitot pressure and yaw angle,[3] 3) surface oil flow including secondary features,[4] and 4) shock structure.[4] Two primary deficiencies of computations are also noted. First, unsteady phenomena, which are inherent to STBLI and of great engineering and scientific importance, are not reproduced by these simulations. The reasons behind this computational deficiency are beyond the scope of this paper: A detailed discussion of the pertinent issues may be found in Ref. 6. The results described in the present effort are, therefore, relevant to those aspects of the computed mean flow structure whose fidelity has been well established as indicated earlier and reconfirmed later. Second, the exhaustive documentation in Ref. 3 suggests that quantitative values of heat transfer rates and skin-friction coefficients are poorly estimated. It is concluded that the primary source of inaccuracy is the turbulence model. Indeed, Fig. 2 indicates that the flow structure is highly three dimensional. The observation that the turbulent mechanisms can be fundamentally different from and without analog in two dimensions (e.g., Ref. 7) suggests that common compressible turbulence models, that is, those not tailored specifically for this flowfield, which are usually straightforward extensions of their two-dimensional incompressible counterparts, may be expected to fail in certain details. Despite this deficiency, that the overall flow features are indeed adequately reproduced has been attributed (see Ref. 3 and the citations therein) to an "approximate triple-deck structure" of the flow. It is this overall flowfield structure that is the focus of this work.

To achieve the stated goals, computational analyses were performed at the U.S. Air Force Research Laboratory (formerly Wright Laboratory). The various cases computed are patterned after the

Presented as Paper 97-1837 at the AIAA 28th Fluid Dynamics Conference, Snowmass Village, CO, 29 June–2 July 1997; received 11 September 1998; revision received 25 April 1999; accepted for publication 3 May 1999.

*Research Aerospace Engineer, Air Vehicles Directorate. Associate Fellow AIAA.
†Senior Scientist, Air Vehicles Directorate. Fellow AIAA.
‡Assistant Professor, Mechanical Engineering Department; currently Assistant Professor, York College of Pennsylvania, York, PA 17405. Member AIAA.
§Senior Research Scientist and Chief of Separated Flows Research Group. Member AIAA.
¶Senior Research Scientist.

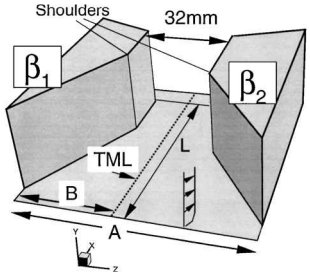

β_1	β_2	A	B
7	7	71.5	35.7
7	11	73.5	35.7
7	15	75.4	35.9
11	11	75.6	37.8
11	15	77.5	38.0
15	15	79.1	39.5

Fig. 1 Double-fin geometry with β_1 and β_2 in degrees, A and B in millimeters, and $L = 166$.

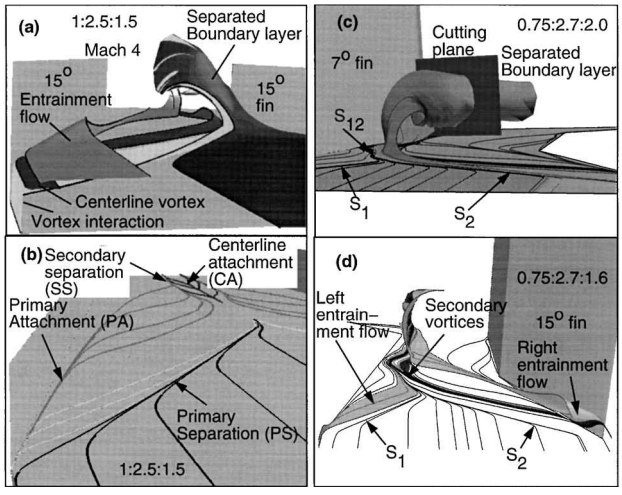

Fig. 2 Coherent structures in separated cases: a) streamribbons for symmetric interaction, b) surface streamlines for symmetric interaction, c) separated boundary-layer ribbon in asymmetric interaction, and d) some other regimes in asymmetric interaction.

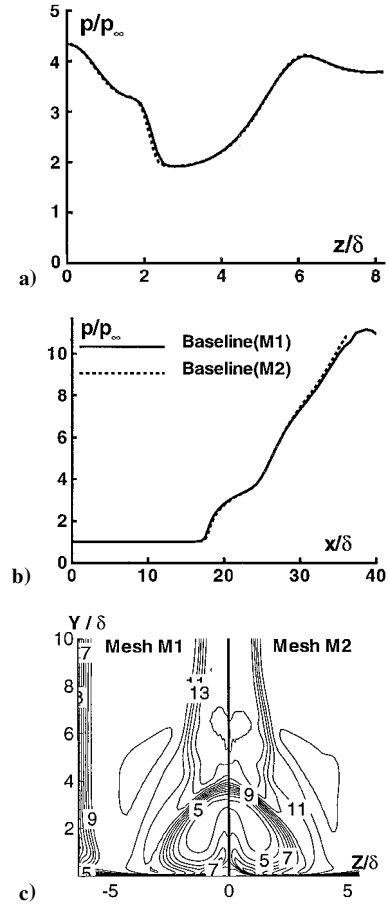

Fig. 3 Effect of mesh resolution (level increment is 0.07 starting with 0.0 at level 1): a) surface pressure on $X = 25.3$ crossflow plane, b) surface pressure on symmetry plane $Z = 0$, and c) pitot pressure (normalized by freestream total pressure) on crossflow plane (from Ref. 17).

experimental test matrix investigated by Zheltovodov et al.[8,9] at the Institute of Theoretical and Applied Mechanics (ITAM), Siberian Division of the Russian Academy of Sciences, Novosibirsk. Planar laser scattering images employed to validate the shock structure of the computations were obtained at Pennsylvania State University.

Theoretical Model

The numerical model consists of the full three-dimensional mean compressible Navier–Stokes equations in strong conservation form and mass-averaged variables. Details may be found in Refs. 10–12 and are not repeated here. Briefly, the inviscid fluxes are evaluated to nominal third-order accuracy with Roe's flux-difference split scheme together with a limiter to enforce monotonicity. Viscous terms are differenced to second-order accuracy in a centered manner. The effects of turbulence are incorporated through the eddy viscosity μ_t assumption and the turbulent Prandtl number is assumed constant at 0.9. The turbulence model employed to derive μ_t is based on the k–ϵ equations[13,14] with low-Reynolds-number terms and incorporating a compressibility correction.

To facilitate validation, the interactions examined experimentally at ITAM by Zheltovodov et al.[8] and Knight et al.[9] are chosen for numerical simulation. The flowfield parameters are Mach 3.95, $P_t = 1.492$ MPa, $T_t = 260.4$ K, and $Re = 87.5 \times 10^6$/m. Six combinations of fin angles 7, 11, and 15 deg are devised to obtain a range of symmetric and asymmetric interactions, as shown in Fig. 1, which arranges the cases by order of increasing inviscid pressure ratio downstream of the intersection of primary shocks.

The boundary conditions are summarized as follows: on solid surfaces, the no-slip condition is enforced, the wall temperature is specified based on experiment, and the normal pressure gradient, k, and ϵ are all assumed zero. The incoming boundary-layer profile is specified at a distance of 4δ ($\delta = 3.5$ mm) upstream of the fin leading edges (FLE) by matching the momentum thickness ($\theta = 0.13$ mm at the FLE) with two-dimensional calculations. The downstream and top boundaries are assumed to be far enough away for the application of simple zero-gradient extrapolation.

The grid is generated as a sequence of nonuniform Cartesian planes normal to the direction of the upstream flow. The clustering is designed to resolve not only the boundary layers and shock waves but also the secondary features of the interior vortical flowfield. Guidelines are taken from extensive previous experience with the present model at field parameters similar to the present.[4,15,16] For example, Fig. 3, taken from Ref. 17, shows surface pressures and pitot pressure contours on a crossflow plane for the 15×15 configuration at the same nominal Mach and Reynolds numbers and incoming boundary-layer properties as in the present work. The meshes designated M1 and M2 in Fig. 3 consist of 9.9×10^5 and 1.9×10^6 points, respectively. It is evident that the relatively coarser mesh is sufficient for the present purpose. Based on these studies, 123 and 88 points are employed in the streamwise ($X = x/\delta$) and normal to the plate directions ($Y = y/\delta$), respectively. The spanwise ($Z = z/\delta$) direction is resolved with 109 points for the symmetric cases, which require only half the domain be computed, and with 197 points for the asymmetric cases. Convergence is ascertained by monitoring several quantities including the global norm, surface pressure, and skin-friction coefficients.

Results

Structure of Asymmetric Interactions

To facilitate description of the asymmetric interactions, the convention followed is to place the fin with the smaller angle to the left when looking downstream. A measure of computational fidelity is established in Fig. 4, which shows surface pressure vs streamwise distance along the throat middle line (TML; Fig. 1) for the three asymmetric configurations. The abscissa and ordinate are normalized by the upstream boundary-layer thickness and the upstream static pressure, respectively. The pressure profile is similar in several

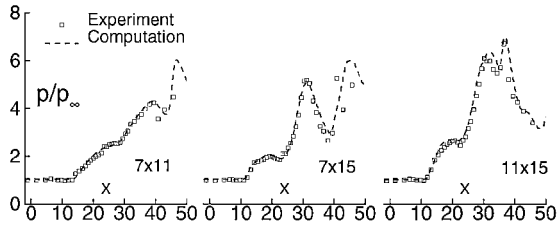

Fig. 4 Surface pressure comparison along TML for asymmetric interactions; experiments of Zheltovodov et al.[8]

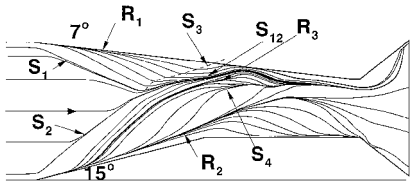

Fig. 5 Computationally simulated surface streamline pattern on plate for 7 × 15 deg interaction.

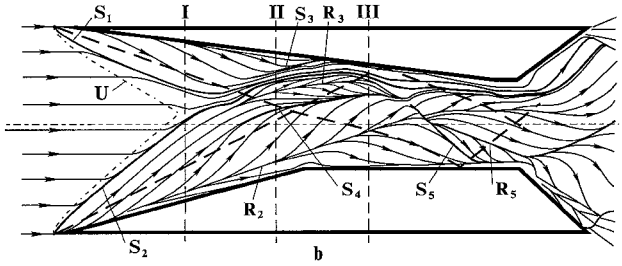

Fig. 6 Experimentally inferred surface streamline pattern from oil flow on plate for 7 × 15 deg interaction.

respects to symmetric interactions and consists of two regions of relatively rapid increase separated by a plateau region, a small decrease in pressure is evident in the 7 × 15 and 11 × 15 deg cases, whose extent increases with interaction strength. The features are captured very accurately by the computations. The excellent agreement may be partly because, as discussed later, unlike for symmetric cases, the TML in downstream regions traverses through regions of relatively benign flow. The discrepancies beyond $X \sim 40$ may be traced primarily to minor differences in downstream duct angle in the computations. On crossflow planes (not shown), all features are reproduced, but errors are modestly higher and similar to those observed in symmetric cases.

To highlight the asymmetric interaction, we focus principally on the 7 × 15 deg case, which has the largest difference in the two fin angles. For this case, the simulated and experimentally inferred plate oil-flow (surface streamline) patterns are presented in Figs. 5 and 6, respectively. For straightforward comparison, the same notation has been employed in both. Each pattern shows several lines of coalescence (S) and divergence (R) that typically indicate separation and attachment, respectively. The two primary lines of coalescence caused by the initial interactions are S_1 and S_2. As the two lines approach each other, the rate of convergence of the upstream flow on these lines diminishes, that is, the lines of coalescence are not as sharply defined. Downstream, these two lines are indistinguishable near the center of the channel: this segment, S_{12} in the simulation, approaches the 7-deg fin reaching a minimum distance at $X \sim 31$ before turning back toward the center of the channel. The primary attachment lines (R_1 and R_2) form near the fin surfaces, as is typical in such interactions. In the experimental inference, a new line S_3 is marked between S_{12} and the 7-deg fin. This line does not form in the computation, though a rapid turning is evident and is shown as a broken line in Fig. 5. A possible mechanism for the presence of S_3 will be apparent in the later discussion of shock structure. The computation and experiment also identify two special lines between S_{12} and the 15-deg fin: one divergent (R_3) and the other convergent (S_4). The pocket between S_{12} and S_4 collapses rather abruptly at $X \sim 36$. Beyond this point, the flow turning angles are similar in the computation and the experiment. However, the latter infers S_5 and R_5, which do not have counterparts in the computation: this aspect is also discussed later with the shock structure. The principal lines, S_1, S_2, R_1, R_2, R_3, and S_4, can be associated with their counterparts in the symmetric interaction shown in Fig. 2b, which employs a different notation for historical reasons. S_1 and S_2 may be identified with the two mirror images of PS, R_1 and R_2 may be similarly associated with PA, R_3 may be associated with CA, and S_{12} and S_4 may be associated with the two mirror images of SS.

The plate oil-flow pattern can be viewed as the footprint of the interaction. Given the analogy with the symmetric interaction, the streamline structure for the 7 × 15 deg configuration can be described in terms of the same four regimes shown in Fig. 2a. Figure 2c shows the separated boundary-layer surface swept out by the flow originating deep inside the incoming boundary layer. On the strong interaction side, the surface rises rapidly in the vicinity of S_2 with particles sweeping spanwise toward the 7-deg fin. The subsequent rollup to form a vortical structure is clearly evident. Particles near the 7-deg fin exhibit relatively little movement away from the surface near S_1 because of the weak nature of that primary interaction, but separate rapidly downstream at S_{12}. The rolled-up separation surface then assumes an orientation parallel to the 7-deg fin.

Some of the other regimes of the 7 × 15 deg interaction are shown in Fig. 2d. These are generally similar to their equivalents in the 15 × 15 deg case with two qualifications: 1) They are no longer symmetric, indeed, because of the nature of the separated boundary layer (Fig. 2c), fluid constituting the two longitudinal vortices originates from the 15-deg side of the incoming boundary layer. 2) The regimes on the weak interaction side are not clearly distinguishable from each other because of the mild nature of the initial interaction, but can nevertheless be defined from their footprints on the plate oil-flow pattern. For example, the vortex interaction regime (not shown) consists of fluid separating from the downstream side of the primary separation line. By definition this regime forms a shear layer with the separated boundary-layer surface of Fig. 2c.

Even though the mean flow is steady, the time-accurate motion of a material line is not intuitively obvious and provides insight into the nature of the mean velocity field. Figure 7 exhibits the position at several time instants of a material line A–B that sweeps out the separated boundary-layer surface of Fig. 2c. The elapsed time between frames is marked in terms of the characteristic time T_c, that is, the time required to traverse the domain at U_∞. The original orientation of this line is assumed to be spanwise, and its trajectory is then derived by convection of the particles constituting this line in a time-accurate manner. In Fig. 7b, the endpoints of the

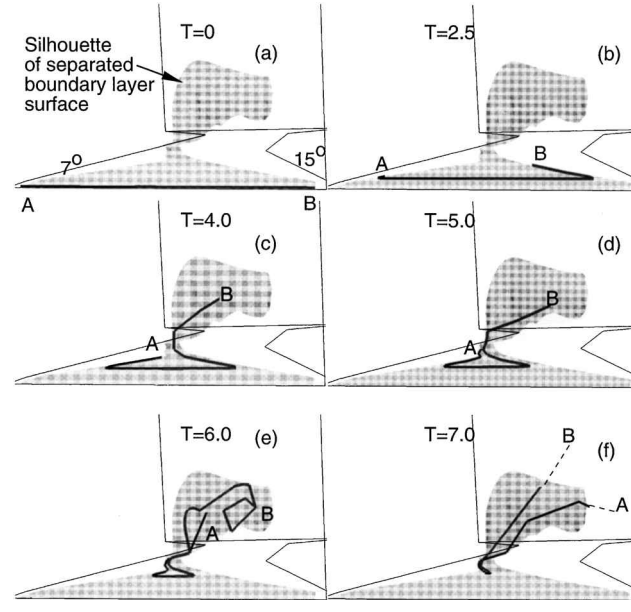

Fig. 7 Convection of a material line sweeping out the separated boundary-layer surface of Fig. 2c.

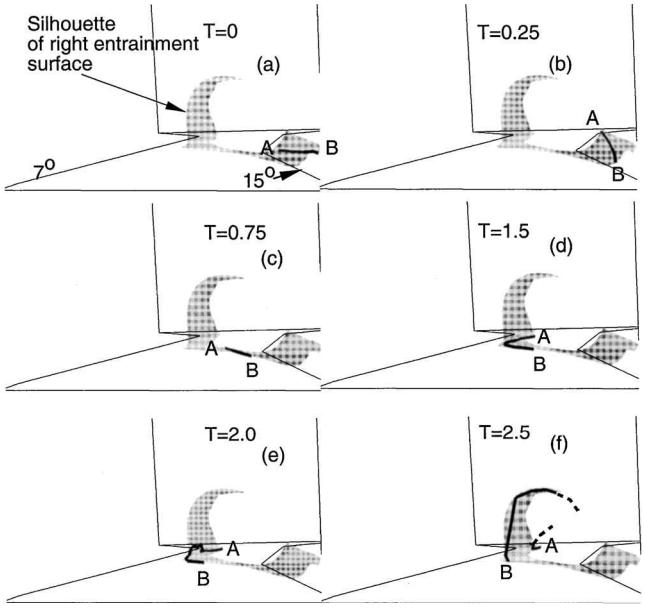

Fig. 8 Convection of a material line sweeping out the right entrainment surface of Fig. 2d.

material line separate from the plate first at its extremities near S_1 and S_2. These ends, particularly end B, are convected away from the plate and toward the center of the channel. This results in a wire-hanger type of structure (Figs. 7c and 7d). The right side of the line then traces a profile of the rolled-up vortical structure defined by the separated boundary layer, Fig. 7e. In Fig. 7f, both endpoints have exited the domain, whereas the low-speed fluid near the center of the channel has not yet separated.

Figure 8 shows the time-accurate motion of a line that sweeps out the right entrainment surface shown in Fig. 2d. The original orientation is spanwise, as shown in Fig. 8a. End B approaches the plate first (Fig. 8b), and its downstream progress is retarded. The material line then assumes a more longitudinal orientation in Fig. 8c, with additional stretching in Fig. 8d. In Fig. 8e, the central portion of the line separates at S_4 (Fig. 5) and is accelerated upward and downstream. Consequently, in Fig. 8f, the line appears in two distinct pieces because the intermediate piece has exited the domain. Because this material line originates in relatively higher speed fluid ($Y \sim 1$), it is transported far more rapidly than that of Fig. 7: Note that the elapsed time between Figs. 8a and 8f is the same as between Figs. 7a and 7b.

A complete understanding of the flowfield is greatly facilitated through a detailed investigation of the shock structure. The fidelity of the computational model in this aspect has been successfully demonstrated in previous studies,[4,16] where a detailed comparison is presented with the experimental inference of Ref. 18. Because of its complicated three dimensionality, the shock structure is typically visualized through its trace on successive crossflow planes. Computationally, this can be accomplished by plotting the magnitude of the pressure gradient ($|\nabla p|$). From this viewpoint, the trace of the shock just downstream of the two FLE appears as two lambda (λ) shocks, each resembling a single-fin interaction. For the 15×15 deg geometry, as the crossflow plane is moved downstream, the traces of the two primary λ appear to cross each other, resulting in a pair of distorted but connected λ systems.[4,18] The shock structure for the 7×15 deg interaction displays several points of similarity. However, sufficient pertinent differences exist, as highlighted later, which serve to illustrate the peculiarities of asymmetric interactions. Planar laser scattering observations obtained at Pennsylvania State University are available for both the 7×15 and the 11×15 deg asymmetric cases. Although the experimental setup for these data was wider than those of the present simulation, the PLS images were further analyzed and qualitatively verify the description to follow.

The trace of the shock is shown at various crossflow planes in Fig. 9. For clarity, the plate and the right (15-deg) fin have been included, the former with its surface oil-flow pattern. The notation employed to denote individual segments of each trace is summarized in Table 1. Briefly, the primary shock systems result in secondary systems after interacting with each other. The secondary systems give rise to tertiary systems after interacting with the side walls. The notation parallels to the extent possible that employed in Refs. 4 and 18 for symmetric interactions. However, for asymmetric cases, it is necessary to distinguish those elements of the shock system that can be clearly identified with one of the two fins. For this purpose, subscripts L and R are employed for the 7- and 15-deg fins, respectively.

Table 1 Numerical notations employed in description of shock structure

Description	Notation[a]
Primary separation shock	1
Primary rear shock	2
Primary inviscid shock	3
Slip line (not shown)	4
Separation vortex (not shown)	5
Secondary separation shock	6
Mach stem	7
Secondary rear shock	8
Secondary inviscid shock	9
Triple point	10a,10b
Expansion	11
Wall-jet shock	12
Bridge shock	13
Rolled-up slip lines (not shown)	14
Tertiary separation shock	15
Tertiary rear shock	16
Tertiary inviscid shock	17
Fin boundary-layer separation shock	18
Fin boundary-layer recompression shock	19

[a]Subscripts L and R indicate elements associated with left and right fins (looking downstream), respectively.

The primary λ systems arising from the two fins are shown in Fig. 9a. Each consists of a separation shock 1, a rear shock 2, and an inviscid shock 3. The strength of each component of the 15-deg system (R) is considerably greater than that of the 7-deg system (L). Not marked are slip lines 4 and the separation vortex 5, which are not discernible as such in the pressure field. Figure 9b shows a station where the two primary separation shocks have crossed. The secondary separation shock associated with the 15-deg fin, shock 6_R, is prominent and develops a curvature. The separation and rear shocks of the 7-deg system are not identifiable at this station. Farther downstream, Fig. 9c, the foot of shock 6_L lies between S_{12} and the 7-deg fin. Close examination reveals a sharp turn in surface oil flow as marked with a dashed line in Fig. 9c at the foot trace of shock 6_R. This shock is the mechanism for the sharp turn in the surface oil flow (Fig. 5) corresponding to the experimentally inferred separation line S_3 in Fig. 6. In Fig. 9d, the primary systems have completely crossed each other. The secondary R system constitutes a distorted λ, whose individual components include in addition to shock 6_R, a secondary rear shock 8_R, both of which are connected to the secondary inviscid shock 9_R by the bridge shock 13_R. Two triple points are evident and are marked 10a and 10b, respectively. This former triple point joins the L system through a Mach stem 7, beneath which lies an expansion 11 (both marked in Fig. 9e instead of Fig. 9d because of space constraints). Stem 7 and expansion 11 also appear as a pair in symmetric interactions (e.g., Ref. 4) and effectively account for the displacement effect of the separated region in the far field. In contrast to the R system, the secondary L system does not display a clear λ structure but simply a mild change of curvature where it is joined with stem 7. This observation is consistent with the conclusions derived from PLS images. Figure 9d also shows the expansion emanating from the shoulder of the 15-deg fin. One of the important features of the entrainment flow is the formation of a wall-jetlike structure shown with the velocity vectors for the right entrainment flow in Fig. 9d. The genesis of this feature is closely linked to the established pressure field as explained in Ref. 4. A new shock 12_R serves to decelerate this wall-jetlike structure and is, therefore, designated the right wall-jet shock. In Fig. 9e, this shock is seen to be coincident with the secondary separation

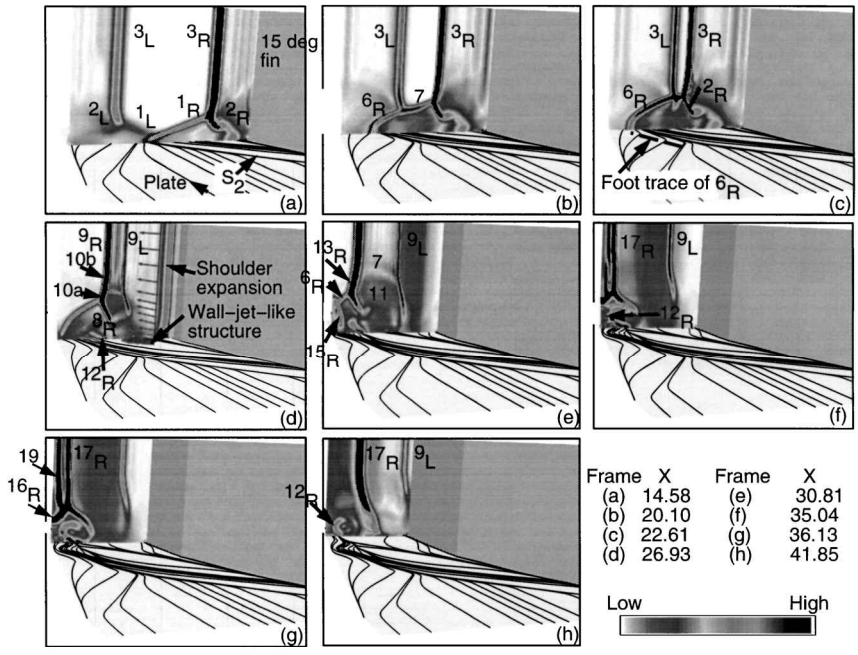

Fig. 9 Shock structure of asymmetric interaction with magnitude of pressure gradient. Each frame has aspect ratio of 0.75:3.8:2.4; see Table 1 for nomenclature.

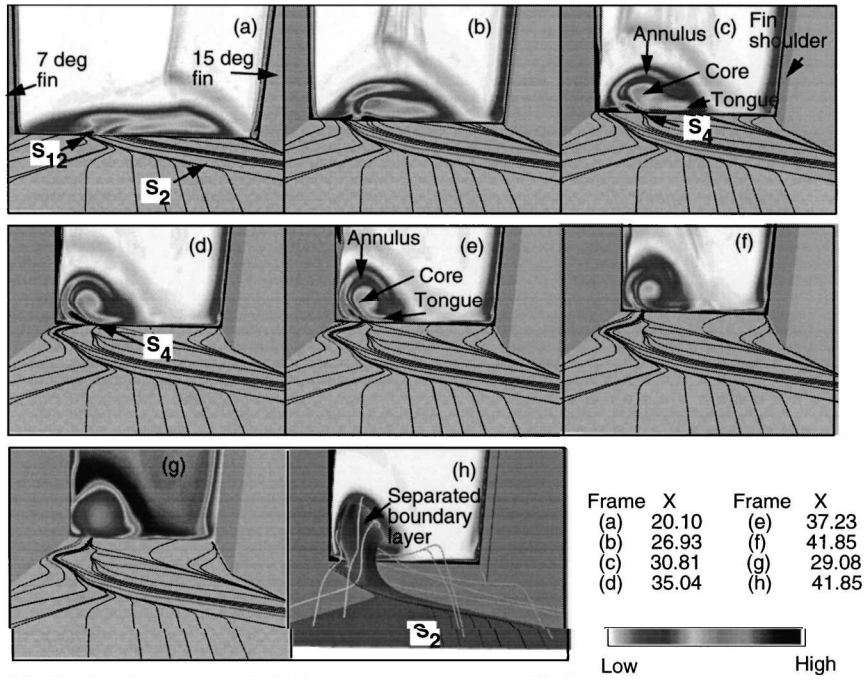

Fig. 10 Nature of the vorticity field and correlation with stagnation pressure and three-dimensional streamline structure.

line S_4 originally introduced in Fig. 5. At this station, shock 6_R encounters the boundary layer associated with the 7-deg fin to form the separation shock 15_R of the tertiary system. Figures 9f and 9g show the tertiary structure after the reflection of the distorted λ off the 7-deg fin is complete. In addition to shock 15_R, the tertiary λ, which is less distorted than the secondary lambda, comprises the rear shock 16_R, and the inviscid shock 17_R. This latter shock shows two closely spaced but nevertheless distinct traces in Figs. 9f and 9g. This effect can be explained by noting that the boundary layer on the 7-deg fin separates in this vicinity, which is also observed in the experiment of Zheltovodov et al.[8]; details of this side wall/shock/vortex interaction are described in Ref. 19. Far enough away from the fin–plate corner, this causes a two-dimensional-like interaction, with associated fin boundary-layer separation shock 18 (not shown) and recompression shock 19. The inviscid shock 9_L weakens due to the interaction with 15-deg shoulder expansion. It is interesting that, if a foot is extrapolated to the surface, it would trace the approximate location of the separation line marked S_5 in Fig. 6, but no line of coalescence forms in the computation. Another prominent downstream feature is the extension and curvature of the wall-jet shock into the field: an effect which will be correlated with the streamline structure in a subsequent paragraph. Finally, in Fig. 9h, the L system also ceases to appear as a λ because most of the shear is restricted to the region near the 7-deg fin, where the extended and curved wall-jet shock persists.

Vorticity is necessarily an important aspect of separated flowfields. Reference 20 contains an enlightening discussion of separation from a vorticity standpoint. There are relatively few observations on the nature of the vorticity field in STBLI. For the single-fin interaction, it has been suggested that the formation of the observed vortical structure can be interpreted as a "reorganization of the spanwise vorticity of the incoming boundary layer."[2] The

vorticity dynamics of supersonic turbulent fields is complex even for the mean flow. We comment next on the established vorticity field, first on its magnitude and later in on its directionality.

The mean vorticity in the incoming two-dimensional boundary layer has only a spanwise component that diminishes monotonically away from the plate. The interaction with the shock wave distorts this profile in a significant fashion. Figures 10a–10f show the vorticity magnitude (looking downstream) at several crossflow planes for the 7 × 15 deg case. Note that the largest values of vorticity occur at the walls. However, the scale has been adjusted to highlight distribution in the interior of the field. The separation surface emanating from each line of coalescence constitutes a shear layer and is accompanied by a sharp penetration of vorticity into the field. For example, in Fig. 10a, this is due to separation at S_{12}, whereas in Fig. 10d, it is caused by secondary separation S_4 associated with the wall-jet shock. Examination of the sequence composed of Figs. 10a–10f reveals the formation of two distinct high vorticity magnitude regions: 1) an inner core region with a tongue extending toward the center of the channel and 2) an outer annular region nearly encapsulating the inner core. In contrast, the stagnation pressure map, shown in Fig. 10g, reveals the presence of a low-energy core very near the 7-deg fin encapsulated near the plate by the high-speed fluid of the entrainment flow. The features of this structure are similar to those observed in symmetric interactions as discussed in, for example, Ref. 4. Scrutiny of Fig. 2c and Figs. 9d–9f indicates that this structure is turned parallel to the 7-deg fin and continues in this direction even though the trace of the outer shock system (see Figs. 9f–9h) displays significant spanwise movement.

These two distinct regions of high vorticity magnitude regions correlate with the particle paths in the flow as shown in Fig. 10h, which displays the vorticity magnitude in the crossflow plane together with the separated boundary layer and a few select streamlines. It is evident that the surface of separation, which intersects the crossflow plane between the two high vorticity regions, can be considered to distinguish the incoming boundary layer into two parts: fluid originating near the strong interaction side forms the inner core while that from the weak interaction side flows over the separation surface to form the outer annulus. Figure 10 also suggests a plausible explanation for the extension of the wall-jet shock into the field as observed in Fig. 9f: This shock is necessary to turn the fluid in the inner vortical core in a direction generally parallel to the 7-deg fin.

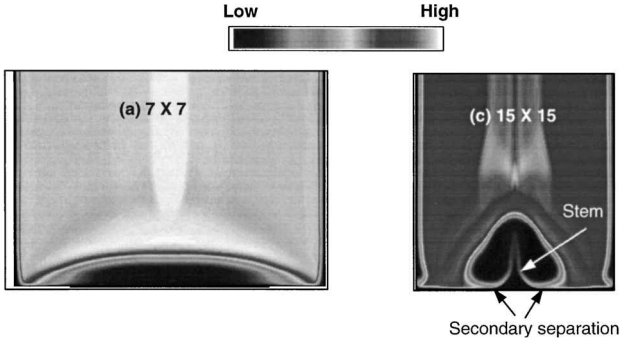

Fig. 11 Evolution of stagnation pressure field in symmetric interactions; crossflow plane located at shoulder of 15-deg fin; $X = 25.89$.

Flowfield Evolution with Interaction Strength

The symmetric computations of the present test matrix provide an opportunity to characterize the evolution of the flowfield with increasing fin angle and, thus, interaction strength. One aspect of practical interest in inlet performance is the stagnation pressure map introduced earlier. Figure 11 shows this quantity for the symmetric 7-, 11-, and 15-deg interactions, respectively, at $X = 25.49$, which is the streamwise location of the 15-deg fin shoulder. The weakest interaction (Fig. 11a) shows relatively mild distortion of the profile but nevertheless shows a pinching effect near the fin surfaces, consistent with the thinning of the shear layer near the corner and entrainment of the higher speed outer flow near the fins. An increase in interaction strength heightens this effect as the central portion of the incoming boundary layer is pushed away from the surface and is encircled by the entrainment flow from the sides. Note that in both the 7- and 11-deg interactions the boundary layer on the symmetry plane is not formally separated in the two-dimensional notion, that is, there is no reversed flow region on the plate. It is evident, however, that this kinematic facet does not preclude the movement of fluid away from the plate. The encirclement by the higher-speed entrained fluid is complete in the 15 × 15 deg interaction, where the effect of the secondary separation is evident in the protrusion of high-stagnation pressure region near the centerline. These form the stem of the so-called mushroom structure observed in the experiments of Ref. 21.

The effect of interaction strength on the vorticity field is shown in Fig. 12 with crossflow plots of its magnitude at two planes and select vortex lines to indicate direction of the vector. Because the upstream vorticity field has only a spanwise component, the typical line traverses from the right (looking downstream) to the left, as shown in Fig. 12a for the 7 × 7 deg flowfield. Downstream of the FLE, vortex lines traverse downward through the right fin boundary layer, sweep spanwise in a distorted fashion, and cross the symmetry plane at a perpendicular, as is required from kinematic constraints. The general appearance of these lines is similar to the so-called hairpin vortices in turbulent flows.[22]

Aspects of the vorticity field for the stronger 15 × 15 deg interaction are shown in Fig. 12b. For clarity, vortex lines are truncated on their trajectory through the fin boundary layers. The vorticity magnitude field has a very different appearance from that for the asymmetric interaction studied earlier (Fig. 10). However, the mushroomlike appearance of the projection on a crossflow plane again permits the identification of two distinct regions: a cap and a stem. This structure is also evident in the downstream station of the 7 × 7 deg interaction. Particle traces indicate that the fluid in the cap originates in the central part of the incoming boundary layer, whereas that in the stem originates nearer the sides and can be associated primarily with entrainment and secondary features. One of the principal features of stronger interactions is an increase in the longitudinal X component of vorticity, particularly in the stem of the mushroom. Consequently, the hairpinlike vortex lines just noted acquire a significant forward inclination. A vortex line of different character, in the sense that it does not resemble a hairpin, is also evident and is marked A in Fig. 12b. This line does not approach the walls but rather exits at the downstream boundary. Some elements of the vortex line structure for the asymmetric 7 × 15 deg interaction are shown in Fig. 12c. The features can be generally characterized as strong on the 15-deg fin side (a significant longitudinal component is evident) and as weak on the 7-deg side.

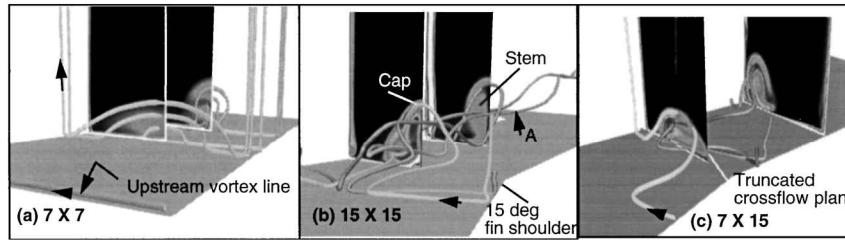

Fig. 12 Structure of vorticity field; some crossflow planes have been truncated to show features of vortex lines.

Conclusion

Asymmetric interactions caused by Mach 4 flow past a double-fin configuration are investigated with particular emphasis on a 7 × 15 deg case. The vortical structure in this interaction is observed to impinge on the side wall and to align itself parallel to the wall. The vorticity field is characterized by the formation of two distinct regions of high magnitude: an inner vortical core and an outer annulus. The surface of separation passes between these two regions and can be perceived as demarcating the incoming boundary layer into two regions. With increasing interaction strength, the pitot pressure map in any crossflow plane shows a pinching effect caused by the entrainment flow from the sides finally transforming into the mushroomlike structure observed in experiment. The evolution of the vorticity field is also described: A principal feature is the increase in the longitudinal component of vorticity with interaction strength.

Acknowledgments

The support of several agencies is gratefully acknowledged. Authors based in the United States were supported by the U.S. Air Force Office of Scientific Research (Monitor, Leonidas Sakell) and by the Major Shared Resource Centers at the Corps of Engineers, Waterworks Engineering Station, the Naval Oceanographic Office, and the Aeronautical Systems Center. Authors affiliated with the Institute of Theoretical and Applied Mechanics were supported by the Russian Foundation for Basic Research (Project Codes 96-01-01777 and 97-01-00885) and the European Office of Aerospace Research and Development (Monitor, C. Raffoul). We gratefully acknowledge the assistance of M. J. Aftosmis, M. S. Maurice, A. M. Shevchenko, and M. R. Visbal.

References

[1]Panaras, A. G., "Review of the Physics of Swept-Shock/Boundary Layer Interactions," *Progress in Aerospace Sciences*, Vol. 31, No. 2/3, 1995, pp. 173–244.

[2]Settles, G. S., and Dolling, D. S., "Swept Shock/Boundary-Layer Intractions: Tutorial and Update," AIAA Paper 90-0375, Jan. 1990.

[3]Knight, D. D., and Degrez, G., "Shock Wave Boundary Layer Interactions in High Mach Number Flows—A Critical Survey of Current CFD Prediction Capabilities," AR-319, Vol. 2, AGARD, 1997.

[4]Gaitonde, D. V., and Shang, J. S., "Structure of a Double-Fin Turbulent Interaction at Mach 4," *AIAA Journal*, Vol. 33, No. 12, 1995, pp. 2250–2258.

[5]Garrison, T. J., Settles, G. S., Narayanswami, N. N., and Knight, D. D., "Laser Interferometer Skin-Friction Measurements of Crossing-Shock-Wave/Turbulent-Boundary-Layer Interactions," *AIAA Journal*, Vol. 32, No. 6, 1994, pp. 1234–1241.

[6]Dolling, D. S, "Problems in the Validation of CFD Codes Through Comparison with Experiment," CP-514, AGARD, 1993, pp. 19-1–19-15.

[7]Bradshaw, P., "Progress in Turbulence Research," AIAA Paper 90-1480, June 1990.

[8]Zheltovodov, A., Maksimov, A., Shevchenko, A., Vorontsov, S., and Knight, D., "Experimental Study and Computational Comparison of Crossing Shock Wave–Turbulent Boundary Layer Interaction," *International Conference on Methods of Aerophysical Research*, Vol. 1, Inst. of Theoretical and Applied Mechanics, Novosibirsk, Russia, 1994, pp. 221–230.

[9]Knight, A., Garrison, T., Settles, G., Zheltovodov, A., Maksimov, A., Shevchenko, A., and Vorontsov, A., "Asymmetric Crossing Shock Wave/Turbulent Boundary-Layer Interaction," *AIAA Journal*, Vol. 33, No. 12, 1995, pp. 2241–2249.

[10]Visbal, M. R., "Structure of Laminar Juncture Flows," *AIAA Journal*, Vol. 29, No. 8, 1991, pp. 1273–1282.

[11]Rizzetta, D. P., "Numerical Investigation of Supersonic Wing-Tip Vortices," AIAA Paper 95-2282, June 1995.

[12]Gaitonde, D. V., Edwards, J. R., and Shang, J. S., "The Computed Structure of a 3-D Turbulent Interaction Caused by a Cylinder/Offset Flare Juncture," AIAA Paper 95-0230, Jan. 1995.

[13]Jones, W. P., and Launder, B. E., "The Prediction of Laminarization with a Two-Equation Model of Turbulence," *International Journal of Heat and Mass Transfer*, Vol. 15, No. 2, 1972, pp. 301–314.

[14]Launder, B. E., and Sharma, B. I., "Application of the Energy Dissipation Model of Turbulence to the Calculation of Flows near a Spinning Disk," *Letters in Heat and Mass Transfer*, Vol. 1, No. 2, 1974, pp. 131–138.

[15]Gaitonde, D. V., Shang, J. S., and Visbal, M. R., "Structure of a Double-Fin Turbulent Interaction at High Speed," *AIAA Journal*, Vol. 33, No. 2, 1995, pp. 193-200; also AIAA Paper 93-3432, Aug. 1993.

[16]Gaitonde, D. V., and Shang, J. S., "On 3-D Shock-Wave/Turbulent Boundary Layer Interactions at Mach 4," AIAA Paper 96-0043, Jan. 1996.

[17]Gaitonde, D. V., and Shang, J. S., "Skin-Friction Predictions in a Crossing-Shock Turbulent Interaction," *Journal of Propulsion and Power*, Vol. 13, No. 3, 1997, pp. 342–348.

[18]Garrison, T. J., and Settles, G. S., "Interaction Strength and Model Geometry Effects on the Structure of Crossing-Shock Wave/Turbulent Boundary-Layer Interactions," AIAA Paper 93-0780, Jan. 1993.

[19]Gaitonde, D. V., Visbal, M. R., Shang, J. S., Zheltovodov, A. A., and Maksimov, A. I., "Parameteric Investigation of Flowfield Structure and Validation Issues in 3-D Crossing-Shock Wave/Turbulent Boundary Layer Interactions," *International Conference on Methods of Aerophysical Research*, Inst. of Theoretical and Applied Mechanics, Novosibirsk, Russia, 1998, pp. 67–76.

[20]Lighthill, M. J., *Attachment and Separation in 3D Flow*, Oxford Univ. Press, Oxford, 1963, Chap. 2.

[21]Garrison, T. J., Settles, G. S., Narayanswami, N. N., Knight, D. D., and Horstman, C. C., "Comparison of Flowfield Surveys and Computations of a Crossing Shock Wave/Boundary Layer Interaction," *AIAA Journal*, Vol. 34, No. 1, 1996, pp. 50–56.

[22]Smith, C. R., Walker, J. D. A., Haidari, A. H., and Sobrun, U., "On the Dynamics of Near-Wall Turbulence," *Philosophical Transactions of the Royal Society of London*, Series A: Mathematical and Physical Sciences, Vol. 336, No. 1641, 1991, pp. 131–175.

P. Givi
Associate Editor